



Oxygen defects-mediated Z-scheme charge separation in $g\text{-C}_3\text{N}_4/\text{ZnO}$ photocatalysts for enhanced visible-light degradation of 4-chlorophenol and hydrogen evolution



Jing Wang ^{a,b,1}, Yi Xia ^{a,c,1}, Hongyuan Zhao ^b, Guifang Wang ^b, Lan Xiang ^{a,*}, Jianlong Xu ^{d,*}, Sridhar Komarneni ^{b,*}

^a Department of Chemical Engineering, Tsinghua University, Beijing 100084, China

^b Department of Ecosystem Science and Management and Materials Research Institute, Materials Research Laboratory, The Pennsylvania State University, University Park, PA 16802, USA

^c Research Center for Analysis and Measurement, Kunming University of Science and Technology, Kunming 650093, China

^d Institute of Functional Nano and Soft Materials (FUNSOM), Jiangsu Key Laboratory for Carbon-based Functional Materials and Devices, Soochow University, Suzhou, Jiangsu 215123, China

ARTICLE INFO

Article history:

Received 9 October 2016

Received in revised form 13 January 2017

Accepted 23 January 2017

Available online 24 January 2017

Keywords:

$g\text{-C}_3\text{N}_4/\text{OD-ZnO}$ catalyst

Z-scheme charge separation

Degradation of 4-chlorophenol

H_2 evolution

Heterojunction interface

ABSTRACT

$g\text{-C}_3\text{N}_4$ nanosheets were coupled with oxygen-defective ZnO nanorods (OD-ZnO) to form a heterojunction photocatalyst with a core-shell structure. Multiple optical and electrochemical analysis including electrochemical impedance spectroscopy, photocurrent response and steady/transient photoluminescence spectroscopy revealed that the $g\text{-C}_3\text{N}_4/\text{OD-ZnO}$ heterojunction exhibited increased visible-light absorption, improved charge generation/separation efficiency as well as prolonged lifetime, leading to the enhanced photocatalytic activities for the degradation of 4-chlorophenol under visible-light illumination ($\lambda > 420$ nm). An oxygen defects-mediated Z-scheme mechanism was proposed for the charge separation in the heterojunction, which involved the recombining of photoinduced electrons that were trapped in the oxygen defects-level of OD-ZnO directly with the holes in the valence band of $g\text{-C}_3\text{N}_4$ at the heterojunction interface. The detection of surface generated reactive species including $\bullet\text{O}_2^-$ and $\bullet\text{OH}$ clearly supported the Z-scheme mechanism. Moreover, the $g\text{-C}_3\text{N}_4/\text{OD-ZnO}$ photocatalysts also exhibited enhanced visible-light Z-scheme H_2 evolution activity, with an optimal H_2 evolution rate of about 5 times than that of pure $g\text{-C}_3\text{N}_4$. The present work not only provided an alternative strategy for construction of novel visible-light-driven Z-scheme photocatalysts, but also gained some new insights into the role of oxygen-defects of semiconductors in mediating the Z-scheme charge separation.

© 2017 Elsevier B.V. All rights reserved.

1. Introduction

Recently, a metal-free semiconductor, graphitic carbon nitride ($g\text{-C}_3\text{N}_4$) has emerged as an attractive material in the fields of environment and sustainability. The facile synthesis, high physicochemical stability and suitable band-gap (~ 2.7 eV) make it a promising visible-light photocatalyst [1,2]. However, the low efficiency of this polymeric photocatalyst caused by the high recombination rate of photoinduced charges limits its practical

application [3,4]. Strategies have been developed to suppress the charge recombination in $g\text{-C}_3\text{N}_4$, such as textural design [5], doping [6] and noble metal loading [7], etc. In particular, coupling $g\text{-C}_3\text{N}_4$ with other semiconductors to form a heterojunction has been widely investigated owing to the efficient spatial separation of charges [2].

Basically, two types of heterojunctions with similar staggered band structure but different pathways for interfacial charge transfer, namely type-II heterojunction and solid-state Z-scheme system, have been well established [8,9]. In a type-II heterojunction, the photoinduced electrons transfer to a less negative conduction band (CB) while the holes to a less positive valence band (VB), leading to their lower redox ability. However, in a Z-scheme system, the photoinduced electrons from less negative CB and holes from less positive VB will recombine at the interface,

* Corresponding authors.

E-mail addresses: xiangan@mail.tsinghua.edu.cn (L. Xiang), xujianlong@suda.edu.cn (J. Xu), sxk7@psu.edu (S. Komarneni).

¹ These two authors contributed equally.

leaving behind the electrons and holes with stronger redox ability separately on two semiconductors. Therefore, the Z-scheme system exhibits dual advantages of efficient charge separation and high redox ability, which are more suitable for the photocatalytic process requiring high redox potentials (especially for H₂ evolution) [8]. Based on this, various g-C₃N₄-based Z-scheme photocatalysts such as g-C₃N₄/TiO₂, g-C₃N₄/BiO₁ and g-C₃N₄/WO₃, etc. have been fabricated and they showed enhanced performances in multiple photocatalytic processes including decomposition of organics, H₂ evolution and CO₂ conversion [10–14]. Nevertheless, to date, g-C₃N₄-based heterojunction photocatalysts are still dominated by the type-II heterojunction. In addition, although an increasing number of g-C₃N₄-based Z-scheme photocatalysts have been recently reported, only a handful of them provided convincible experimental evidences to support the proposed mechanisms [1]. Given these conditions, it is still desirable to develop novel strategies for construction of g-C₃N₄-based Z-scheme photocatalysts as well as explore their interfacial charge separation mechanism.

Another main drawback of g-C₃N₄ is its limited adsorption edge of 460 nm. When constructing a g-C₃N₄-based Z-scheme photocatalyst, the visible-light utilization ability of the other component should be considered. Many g-C₃N₄-based Z-scheme systems containing wide-band semiconductors such as TiO₂, ZnO and BiOCl, etc. usually need to work efficiently under UV illumination [10,13,15,16]. On the other hand, some narrow band-gap semiconductors used in the Z-scheme system, such as CdS and Ag₃PO₄ [17,18], etc. are unfortunately unstable and suffer from serious photodecomposition. Therefore, many efforts have been devoted to the coupling of g-C₃N₄ with band-engineered semiconductors for improved visible-light absorption. For example, g-C₃N₄ was hybridized with S-doped TiO₂ [19] or N-doped ZnO [20] to form Z-scheme photocatalysts with enhanced visible-light absorption, which were attributed to the formation of dopants-isolated energy levels in TiO₂ and ZnO. In addition to foreign elemental doping, introducing defects as “self-doping” to create defects-isolated levels in semiconductors is an alternative approach to extend light absorption. Specially, the oxygen defects have been demonstrated to be effective in adjusting the band levels of many metal oxides-bearing Z-scheme systems [21–25]. For example, various semiconductors with rich oxygen vacancies such as Bi₂₀TiO₃₂ [24], ZnO [22], SnO_{2-x} [23,25] etc., were coupled with g-C₃N₄ and the obtained Z-scheme heterojunction showed enhanced visible-light photocatalytic degradation of organics and CO₂ reduction. It was generally suggested that oxygen-defective metal oxides extended the visible-light absorption owing to their defects-induced band gap narrowing. However, in these reported g-C₃N₄-based heterojunction systems, the critical roles of oxygen defects in mediating the Z-scheme charge separation were not fully identified. Further insight into the interfacial charge transfer mechanisms will facilitate the construction of visible-light-driven Z-scheme photocatalysts by employing oxygen defects.

Herein, g-C₃N₄ nanosheets were coupled with oxygen-defective ZnO nanorods (OD-ZnO) to form a core-shell heterojunction. The rich surface oxygen vacancies in OD-ZnO played dual-function roles of improving visible-light absorption and mediating the Z-scheme charge separation. Multiple optical and electrochemical analyses were employed to evaluate the charge separation efficiency of the heterojunction, and the Z-scheme mechanism was convinced by detecting the surface generated reactive species. The enhanced charge generation and separation efficiency of the g-C₃N₄/OD-ZnO photocatalysts led to their superior-visible-light activities for degradation of 4-chlorophenol. Moreover, the oxygen defects-mediated Z-scheme H₂ evolution from a g-C₃N₄-based photocatalyst was demonstrated for the first time.

2. Experimental

2.1. Synthesis of photocatalysts

Commercial chemicals of analytical grade and deionized water with a resistivity $>18 \text{ M}\Omega \text{ cm}^{-1}$ were used in all the experiments. Commercial ZnO powder (denoted as C-ZnO, >99.9%) with few defects was used as a reference in this work and was purchased from Sigma-Aldrich.

Oxygen-defective ZnO nanorods (OD-ZnO) were synthesized from ε -Zn(OH)₂ precursor by a solution conversion method based on our previous work with modifications [26]. In brief, ε -Zn(OH)₂ was prepared by drop-wise addition of 50 mL of 2.0 mol L⁻¹ ZnSO₄ into 50 mL of 4.0 mol L⁻¹ NaOH at 25 °C under stirring. The precipitate was filtrated, washed with deionized water and dried at 25 °C for 24 h. 3.50 g of ε -Zn(OH)₂ was dispersed in 40.0 mL of 4.0 mol L⁻¹ NaOH solution, then the slurry was kept at 80 °C for 0.5 h. The final OD-ZnO product was filtrated, washed and dried at 60 °C for 12 h.

Bulk g-C₃N₄ was prepared by heating urea to 550 °C in a covered crucible with a heating rate of 5 °C min⁻¹ and kept isothermally at 550 °C for 3 h [27]. 50 mg of bulk g-C₃N₄ powder was ultrasonically exfoliated into thin nanosheets in 50 mL of water for 4 h. To this dispersion, an appropriate amount of OD-ZnO was added and then stirred at room temperature for 48 h. After complete evaporation of the water, g-C₃N₄/OD-ZnO composite powders left in the beaker were collected and dried at 60 °C for 12 h. Samples with x% (weight ratio) loaded g-C₃N₄ were denoted as CN-x/OD-ZnO.

2.2. Characterization

The morphology and microstructure of the samples were examined with a field emission scanning electron microscope (FESEM, Nova NanoSEM 630, FEI Company, USA) and a high-resolution transmission electron microscope (HRTEM, JEM-2010, JEOL, Japan) equipped with energy-dispersive X-ray spectroscopy. Powder X-ray diffraction (XRD) was used for phase identification using an X-ray powder diffractometer (PANalytical Empyrean, USA) with CuK α ($\lambda = 0.154178 \text{ nm}$) radiation. Raman spectra were recorded using He-Ne laser excitation at 532 nm with a Horiba Jobin Yvon LabRAM HR800 Raman spectrometer. Surface composition of the samples was characterized by X-ray photoelectron spectrometer (XPS, PHI-5300, PHI, USA). Electron-spin-resonance (ESR) measurements were performed on a JEOL-TE300 spectrometer operating at an X-band frequency of 9.4 GHz. UV-vis diffuse reflectance spectra were recorded on a Perkin-Elmer Lambda 950 UV-vis-NIR spectrophotometer. The functional groups of the samples were examined by a Fourier transform infrared spectrometer (FT-IR, Nexus, Nicolet, USA). The composition of the samples was determined by thermogravimetry (TG, NETZSCH STA 409C, Switzerland) under nitrogen atmosphere with a heating rate of 10 °C min⁻¹. The Brunauer–Emmett–Teller (BET) surface areas of the products were determined using a nitrogen adsorption analyzer (Quadasorb-S1, Quantachrome, USA) and the pore-size distribution was estimated by the Barrett–Joyner–Halenda method. Photoluminescence (PL) spectra and PL decay curves of the samples were measured at room temperature on a FLS920 fluorescence lifetime spectrophotometer (Edinburgh Instruments, UK) under the excitation of a LED lamp with an excitation wavelength of 400 nm.

2.3. Photoelectrochemical measurements

The photocurrent responses were measured in a three-electrode quartz cell with 0.1 mol L⁻¹ Na₂SO₄ electrolyte solution and recorded using an electrochemical system (CHI-660 B workstation,

CH Instruments). A Xe lamp with a Y-43 cutoff filter ($\lambda > 420$ nm) was used as the visible light source (light intensity: 1 mW cm^{-2}). The working electrodes were prepared by drop-casting of the photocatalyst suspensions (10 mg mL^{-1}) onto Ti foil and drying at 60°C for 12 h. Platinum wire and Ag/AgCl were used as the counter and reference electrodes, respectively. The electrochemical impedance spectroscopy (EIS) measurements were performed in a three-electrode cell in the presence of $5\text{ mM }[\text{Fe}(\text{CN})_6]^{3-}/[\text{Fe}(\text{CN})_6]^{4-}$ by applying an AC voltage with 5 mV amplitude in a frequency range from 0.01 Hz to 100 kHz under open circuit potential conditions.

2.4. Evaluation of photodegradation activity

The photocatalytic activities were evaluated by the degradation of 4-chlorophenol (4-CP) under visible light. A 300 W Xenon lamp with a Y-43 cutoff filter (Asahi Techno Glass, $\lambda > 420$ nm) was used as the visible light source. The spectral distributions of light from the Xenon lamp and the light passing the Y-43 filter were recorded by using a spectro-radiometer (USR-40D, Ushio Ltd) and provided in Fig. S1, revealing that the Y-43 filter could block the light at $<420\text{ nm}$ but would not obviously affect the light in the visible region (420–780 nm). In a typical run, 0.1 g of the photocatalyst was dispersed in 100 mL of 4-CP aqueous solution ($10^{-4}\text{ mol L}^{-1}$), stirred in the dark for 30 min to achieve the adsorption-desorption equilibrium and then illuminated under visible light. The suspensions were sampled at regular intervals (10 or 15 min) and centrifuged to remove the catalysts at 5000 rpm for 10 min. The supernatant was filtrated through a $0.45\text{ }\mu\text{m}$ filter and then analyzed by a high performance liquid chromatograph (HPLC, Shimadzu) equipped with a UV-vis detector and a C18 column. The mobile phase (1 mL min^{-1}) was composed of methanol and H_2O ($\text{v/v}=6:4$), and $20\text{ }\mu\text{L}$ of the sample solution was injected. The initial concentrations (C_0) for the calculation of rate constants were considered to be the 4-CP concentration after adsorption equilibrium. The extent of mineralization of 4-CP was measured using a total organic carbon (TOC) analyzer (Shimadzu TOC-V CPN).

2.5. Detection of reactive species

DMPO in methanol was used for the detection of superoxide radicals (DMPO- $\bullet\text{O}_2^-$). 10 mg samples and $40\text{ }\mu\text{L}$ DMPO were dispersed in 0.5 mL CH_3OH by stirring for 5 min. After 30 s illumination, ESR signals of DMPO- $\bullet\text{O}_2^-$ species were recorded with a JEOL-TE300 spectrometer. Nitroblue tetrazolium (NBT) degradation was also used to quantitatively determine the generated $\bullet\text{O}_2^-$. The method was also similar to the former experiment with NBT replacing the pollutant, and the concentration of NBT was $2.5 \times 10^{-2}\text{ mM}$. PL spectra were used to disclose the formation of $\bullet\text{OH}$ using terephthalic acid (TA) as a probe molecule. Photocatalyst (0.05 g) was dispersed in a 40 mL of the TA ($5 \times 10^{-4}\text{ mol L}^{-1}$) aqueous solution with NaOH ($2 \times 10^{-3}\text{ mol L}^{-1}$) at room temperature. The suspension was illuminated under visible light for 30 min, then the PL spectra of the suspension were measured using a FLS920 fluorescence spectrophotometer with excitation wavelength of 365 nm .

2.6. Photocatalytic H_2 evolution measurements

The photocatalytic hydrogen evolution was carried out in a 250 mL sealed three-necked Pyrex flask at room temperature and atmospheric pressure. A 300 W Xenon lamp equipped with a Y-43 cutoff filter ($\lambda > 420$ nm) served as the visible-light source. In a typical run, 0.1 g of catalyst was dispersed in 100 mL of 10 vol\% triethanolamine (TEOA) aqueous solution, and then bubbled with argon for 30 min to remove the dissolved oxygen. Certain amount of H_2PtCl_6 was pre-dissolved into the reactant suspension for in-

situ photo-deposition of Pt as a co-catalyst (1 wt%) on the catalysts by UV irradiation for 30 min. The suspension was then exposed to visible light with continuous stirring. 0.5 mL of gas was sampled at regular intervals (2 h) through the septum, and hydrogen was analyzed by a gas chromatograph (GC-Agilent 7890A, with nitrogen as a carrier gas) equipped with a 5 \AA molecular-sieve column and a thermal-conductivity detector.

3. Results and discussion

Oxygen-defective ZnO nanorods (OD-ZnO) were simply synthesized by a solution-conversion approach using $\varepsilon\text{-Zn(OH)}_2$ as precursor. Fig. 1 shows that the OD-ZnO displays a needle-like morphology with diameters of $50\text{--}200\text{ nm}$ and lengths of $0.5\text{--}4\text{ }\mu\text{m}$. The XRD pattern (Fig. S2) reveals the hexagonal wurtzite structure. A few damaged domains (marked by dashed yellow circles) could be observed in the HRTEM image of the nanorods (Fig. 1b). Such a lattice deformation should be mainly caused by the surface reconstruction or the existence of defects [28]. Correspondingly, the SAED analysis (inset in Fig. 1b) showing an irregular pattern also indicates the existence of the lattice disorder. Multiple characterization techniques were further employed to identify the oxygen-defective nature of the as-prepared ZnO nanorods using commercial ZnO powder (Fig. S3, C-ZnO) as a reference. The Raman spectra (Fig. 1c) indicates that the $\text{E}_1(\text{LO})$ modes (located at 582 cm^{-1}) of OD-ZnO exhibited a much higher intensity compared to C-ZnO, which were generally assigned to the oxygen deficiencies such as oxygen vacancies (V_0) in ZnO [29]. Fig. 1d shows the high-resolution O1 s spectra of the two samples. Two species centered at the banding energies of ca. $530.2\text{--}530.3\text{ eV}$ and $531.6\text{--}531.7\text{ eV}$ were denoted as O1 and O2, respectively. The species of O1 were originated from the lattice oxygen anions (O^{2-}) in wurtzite structure, while the species of O2 belonged to the O_x^- ions (mainly O_2^-) in the oxygen-defective regions caused by V_0 on the surface [30]. The ratios of O2 species on the surface of OD-ZnO and C-ZnO were 43.6 and 12.4%, respectively, indicating that the OD-ZnO had a high concentration of surface oxygen vacancies. In addition, the ESR spectra (Fig. 1e) of OD-ZnO displayed a significant signal with $\text{g-factor} = 2.008$, which was not observed for C-ZnO and could be attributed to an unpaired electron trapped in a surface oxygen vacancy site [31]. All the results presented above confirmed the existence of a high concentration of oxygen vacancies in the OD-ZnO, especially on the surfaces. The oxygen-defective nature of the ZnO nanorods would affect their optical properties such as the absorption characteristics. The UV-visible diffuse reflectance spectra (DRS) in Fig. 1f revealed that C-ZnO only absorbed the light with $\lambda < 420\text{ nm}$ owing to the intrinsic wide band gap, while the absorption curve of OD-ZnO exhibited an obvious red shift to longer wavelength compared to C-ZnO reference, implying the band gap narrowing of OD-ZnO. The large absorption tail occurring in the visible-light regions of OD-ZnO was attributed to the rich oxygen vacancies which generated a defects-isolated level below the CB of ZnO [32,33]. Therefore, the visible-light absorption capacity was highly increased in OD-ZnO.

The as-prepared bulk $\text{g-C}_3\text{N}_4$ was firstly exfoliated into thin nanosheets to help the subsequent self-assembly process. After long-time sonication in water, dispersible $\text{g-C}_3\text{N}_4$ nanosheets with sizes less than 100 nm and thicknesses down to nanometers were obtained (Fig. 2a). $\text{g-C}_3\text{N}_4/\text{OD-ZnO}$ heterostructures with varying $\text{g-C}_3\text{N}_4$ ratios were simply prepared by adding an appropriate amount of OD-ZnO into the $\text{g-C}_3\text{N}_4$ nanosheets suspension followed by a solvent evaporation-induced self-assembly process [34]. The ratios of $\text{g-C}_3\text{N}_4$ in the nanocomposites could be simply adjusted by tuning the adding amount of ZnO and were also confirmed by TG analysis (Fig. S4). The SEM image (Fig. 2b) reveals

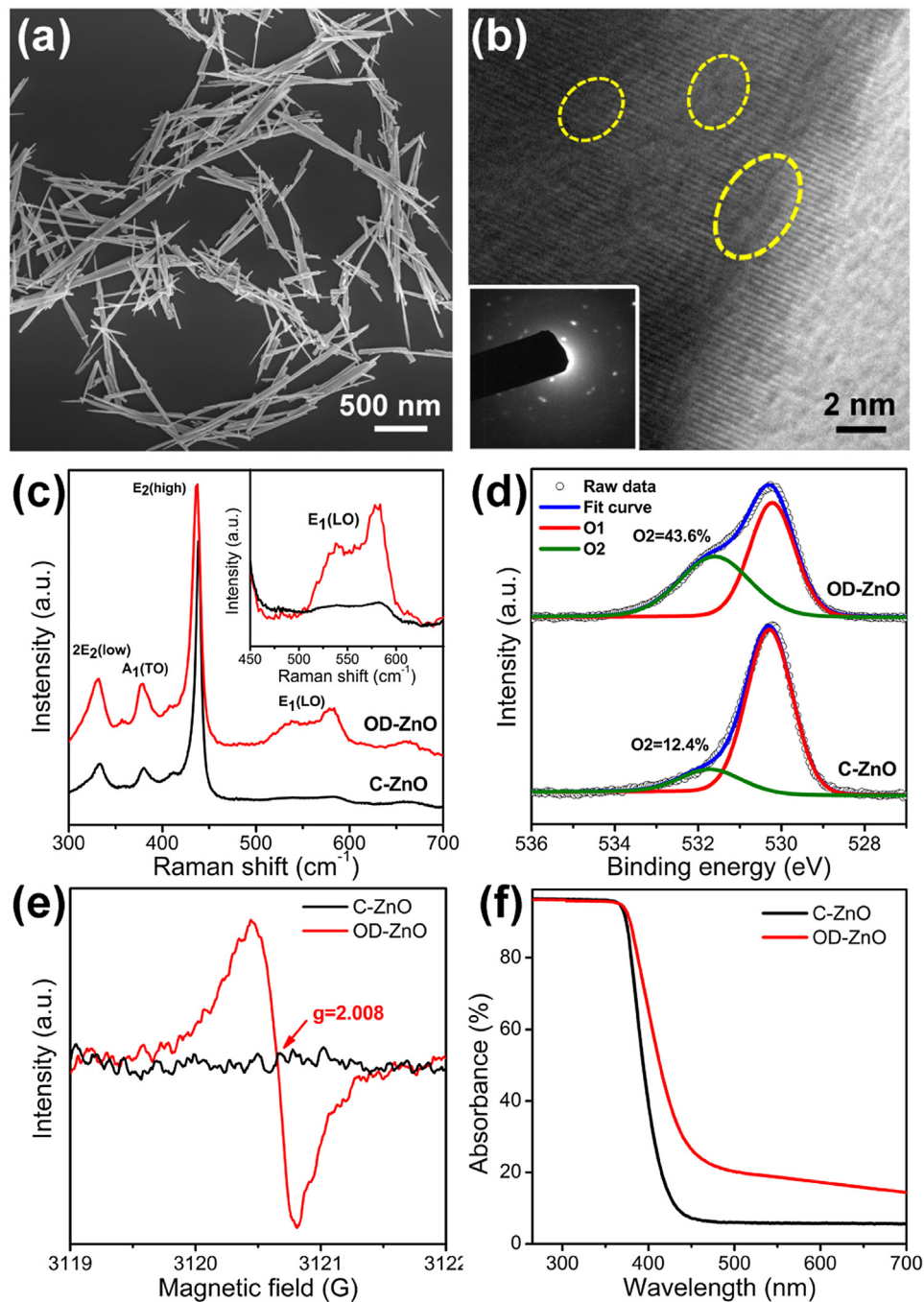


Fig. 1. Characterizations of the as-prepared OD-ZnO. SEM (a) and TEM (b) images; Raman spectra (c), high-resolution O1s XPS spectra (d), ESR spectra (e), UV-vis diffuse reflectance spectra (f) of OD-ZnO, using commercial ZnO powder (C-ZnO) as a reference. (For interpretation of the references to colour in the text, the reader is referred to the web version of this article.)

a typical composite sample containing 10 wt% g-C₃N₄ (denoted as CN-10/OD-ZnO), which exhibited a morphology similar to the original nanorods. However, high-magnification SEM image (inset in Fig. 2b) indicates that the g-C₃N₄ nanosheets seem to coat onto the ZnO nanorods, resulting in rough surfaces of the nanorods. The phase and composition of the g-C₃N₄ nanosheets and the obtained g-C₃N₄/ZnO heterostructures were confirmed by the XRD patterns as displayed in Fig. 2c. The TEM image (Fig. 2d) of a single composite nanorod clearly reveals the coating of g-C₃N₄ nanosheets onto a ZnO nanorod to form a core-shell structure with a shell thickness of ca. 10 nm. The lattice structures of the ZnO core and g-C₃N₄ shell were analyzed by HRTEM. Two different interplanar spacings

of 0.26 and 0.325 nm were observed, corresponding to the (001) plane of ZnO and (002) plane of g-C₃N₄, respectively. In addition, the EDS mapping analysis presented in Fig. 2e demonstrated that the core of a nanorod tip was mainly composed of zinc and oxygen elements, while the shell was mainly composed of nitrogen, further confirming the core-shell structure. The shell thickness of the heterostructures depended on the ratio of g-C₃N₄ in the nanocomposites. As demonstrated in Fig. S5, for CN-5/OD-ZnO sample, the g-C₃N₄ nanosheets could not fully cover the ZnO nanorods surface, while for CN-20/OD-ZnO sample, the g-C₃N₄ nanosheets formed a continuous shell with a larger thickness of 20 nm. The self-assembly of core-shell structures should be attributed to the minimization of

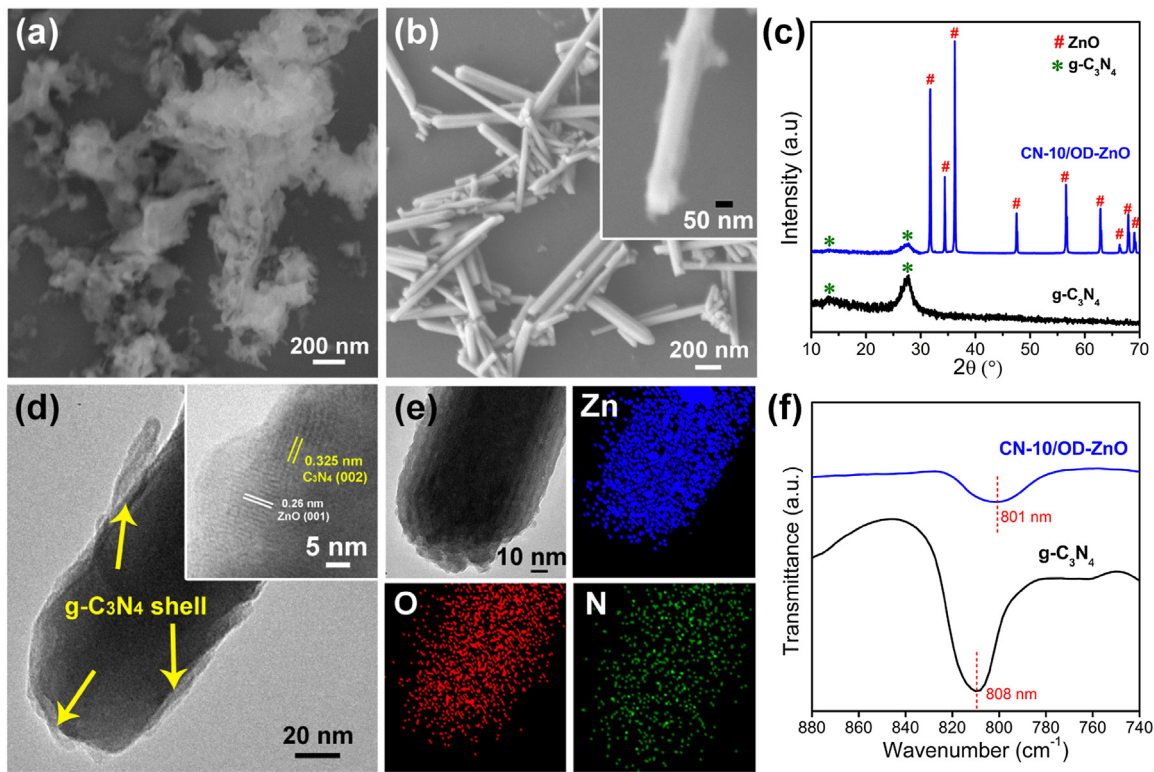


Fig. 2. SEM images (a, b), XRD patterns (c), FT-IR spectra (f) of the exfoliated $\text{g-C}_3\text{N}_4$ nanosheets (a) and typical $\text{g-C}_3\text{N}_4/\text{ZnO}$ heterostructures (CN-10/OD-ZnO); TEM image, HRTEM image (inset) (d) and corresponding EDS mapping images (e) of CN-10/OD-ZnO sample.

the surface energy of the exfoliated thin $\text{g-C}_3\text{N}_4$ nanosheets during the solvent evaporation. Moreover, strong chemical interactions were believed to occur between $\text{g-C}_3\text{N}_4$ and ZnO according to FT-IR analysis (Fig. 2f). The peak at 808 cm^{-1} in pure $\text{g-C}_3\text{N}_4$ relating to the s-triazine ring vibrations [35] shifted to a lower wavenumber (801 cm^{-1}) in the core-shell heterostructures, suggesting the possible formation of chemical bonds between C_3N_4 and ZnO . This strong interaction would not only facilitate the formation of robust core-shell structures, but may also promote the interfacial charge transfer in the photocatalytic processes.

Fig. S6 gives the high-resolution XPS spectra of C 1s, N 1s, Zn 2p and O 1s of CN-10/OD-ZnO sample. The peak at 284.6 eV is ascribed to adsorbed adventitious carbon, whereas the other peak at 287.5 eV corresponds to the sp^3 -bonded C in $\text{C}=\text{N}-\text{N}$ coordination. Two major peaks at 398.5 and 399.3 eV deconvoluted from N 1s peaks belong to the pyridinic-like nitrogen and graphite nitrogen, respectively. It was also noticed that the ratios of O2 species further increased to 55.3%, indicating increased surface defects could be aggregated at the solid–solid contact interface. The contact interfaces derived from defect-rich ZnO surfaces may serve as the recombination center of photoinduced electron-hole pairs and thus leading to the formation of the Z-scheme system [8], which will be discussed in detail in the later part.

The BET surface areas of three typical samples including $\text{g-C}_3\text{N}_4$ nanosheets, OD-ZnO and CN-10/OD-ZnO were also investigated, as shown in Fig. S7. The $\text{g-C}_3\text{N}_4$ nanosheets had a low surface area of $10\text{ m}^2/\text{g}$ and the OD-ZnO showed a comparatively larger surface area of $15\text{ m}^2/\text{g}$. The core-shell CN-10/OD-ZnO heterostructure exhibited a much larger surface area of $38\text{ m}^2/\text{g}$. The exfoliated $\text{g-C}_3\text{N}_4$ nanosheets would easily re-stack into thick layers and lose their surface area, leading to a low BET value. The coating of $\text{g-C}_3\text{N}_4$ nanosheets onto ZnO nanorod surfaces in the form of thin shells could inhibit their re-stacking during the drying process. In addition, the IR results (Fig. 2f) reveal the possible formation of chemical

bonds between ZnO and $\text{g-C}_3\text{N}_4$, which improved the robustness of the nanocomposites. Therefore, the self-assembled formation of a $\text{g-C}_3\text{N}_4/\text{ZnO}$ core shell structure not only led to a well-defined solid–solid interface, but also contributed to the increased surface area of the nanocomposites.

A combined analysis of UV-vis DRS, electrochemical impedance spectroscopy (EIS) and photocurrent measurements were carried out to investigate the performances of charge generation, transfer and separation of the heterojunction, as shown in Fig. 3. As expected, the C_3N_4 sample shows its absorption edge around 460 nm , corresponding to its band gap of $\sim 2.7\text{ eV}$, while the absorption edge of $\text{g-C}_3\text{N}_4/\text{OD-ZnO}$ samples experience a red shift and an increased absorption in the visible-light region (Fig. 3a) owing to the visible-light active OD-ZnO. For EIS analysis, the semicircle part at higher frequencies corresponds to the electron-transfer-limited process, and the semicircle diameter is equivalent to the electron-transfer resistance (R_{et}) [36]. Fig. 3b indicated that the R_{et} value of the $\text{g-C}_3\text{N}_4$ nanosheets and OD-ZnO were about 250 and $170\text{ }\Omega$, respectively, while the $\text{g-C}_3\text{N}_4/\text{OD-ZnO}$ nanocomposite samples exhibited comparatively lower R_{et} values, and the R_{et} order was $\text{CN-10/OD-ZnO} < \text{CN-20/OD-ZnO} < \text{CN-5/OD-ZnO} < \text{OD-ZnO} < \text{g-C}_3\text{N}_4$, suggesting that the electroconductivity was improved by the heterojunction. As discussed in the former parts, strong chemical interaction as well as a large number of defects may be generated at the $\text{g-C}_3\text{N}_4/\text{OD-ZnO}$ interface, thus the solid–solid contact may have quasi-continuous energy levels and show similar properties to conductors [8], leading to the low electrical resistance of the heterojunction.

Fig. 3c shows the photocurrent responses of samples tested on a photoelectrochemical test device with visible light ($\lambda > 420\text{ nm}$) on and off cycles. Though possessing a good visible light absorption ability, $\text{g-C}_3\text{N}_4$ electrode showed a weak photocurrent response due to its high electric resistance, while the OD-ZnO electrode showed a higher photocurrent response because of its smaller

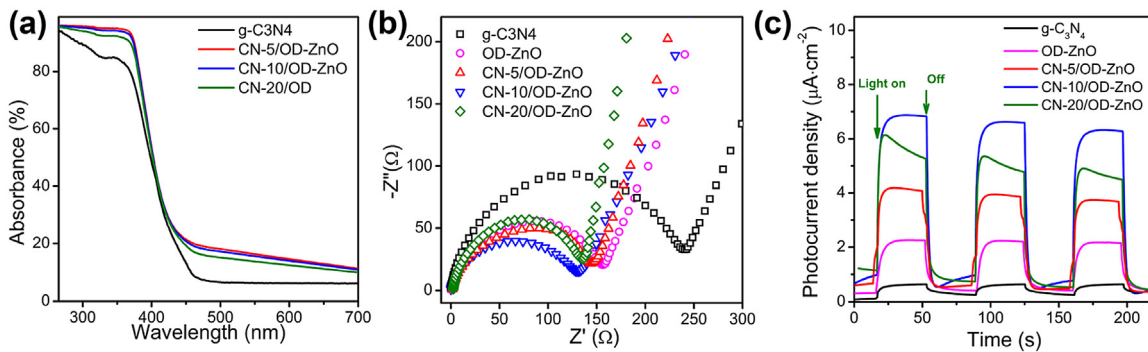


Fig. 3. (a) UV-vis diffuse reflectance spectra of g-C₃N₄ and CN-x/OD-ZnO; (b) EIS Nyquist plots of g-C₃N₄, OD-ZnO and CN-x/OD-ZnO samples; (c) photocurrent response of the g-C₃N₄, OD-ZnO and CN-x/OD-ZnO electrodes under the irradiation of visible-light ($\lambda > 420$ nm); x = 5, 10, 20.

resistance. The g-C₃N₄/OD-ZnO electrodes exhibited enhanced photocurrent responses and the response order was consistent with the order of R_{et} value. The CN-10/OD-ZnO electrode showed largest photocurrent response, about 3 and 8 times higher than that of OD-ZnO and g-C₃N₄, respectively. These suggested that the g-C₃N₄/OD-ZnO heterojunction led to improved visible light absorption and electroconductivity, which are expected to have enhanced generation, transfer and separation efficiency of photoinduced carries under visible-light illumination and this would be beneficial for the visible-light photocatalytic activity.

Steady-state and transient photoluminescence (PL) analyses were performed to further investigate the charge transfer and separation in the heterojunction, as shown in Fig. 4. Considering that intrinsic ZnO has a band-gap of 3.3 eV, 400 nm excitation light was employed herein for PL measurements, thus the direct excitation of the electrons from VB to CB of OD-ZnO would be inhibited under this condition [37]. As shown in Fig. 4a, OD-ZnO shows a broad-band of green emissions centered at ca. 520 nm, which were generally considered originating from singly charged oxygen vacancies (V_O^\bullet), consisting with the ESR result in Fig. 1e since V_O^\bullet is paramagnetic. To determine the energy band structure of OD-ZnO, the valence band XPS spectrum (VB-XPS) was also measured, as shown in Fig. S8. The OD-ZnO sample displayed a VB with the edge of the maximum energy around 2.5 eV, similar to that of bulk ZnO (~2.6 eV), indicating that the oxygen-defective nature did not significantly affect the VB position of OD-ZnO. Therefore, the green emission at ~520 nm, which corresponded to an energy of ca. 2.4 eV, should have originated from the recombination of the photoexcited holes in VB and the photoexcited electrons that were being trapped in the V_O -isolated states of about 0.8 eV below the CB of ZnO [38–40]. Moreover, the PL results of OD-ZnO implied that under visible-light illumination (400 nm), the photoexcited electrons were preferably trapped in the V_O state rather than being further excited to the CB band, since no obvious UV emission from OD-ZnO was observed. The energy band structure and PL emission mechanism of OD-ZnO were summarized in Fig. S9, which are consistent with previous studies [41–43]. For comparison, the C-ZnO sample, however, did not show obvious emissions under 400 nm excitation, but only exhibited a strong UV emission located at 384 nm under 325 nm excitation (Fig. S10). The above results indicated that the V_O -isolated state in the band structure of OD-ZnO was responsible for visible-light absorption and the green PL emission under 400 nm excitation. It will be also demonstrated later that the V_O -isolated state was critical for the formation of the Z-scheme system.

The pure g-C₃N₄ nanosheets exhibited a strong emission peak at around ~460 nm under 400 nm excitation, which is consistent with the band gap of 2.7 eV, and the high intensity of the emission peak indicated the high charge recombination rate in pure

g-C₃N₄. However, the g-C₃N₄/OD-ZnO heterojunction showed a much weaker emission peak centered at around 490 nm, which could be divided into two component emission peaks belonging to g-C₃N₄ and OD-ZnO (inset in Fig. 4a), respectively. The intensity of the two peaks dropped significantly compared to pure g-C₃N₄ and OD-ZnO, suggesting that the recombination of photoinduced charges in g-C₃N₄ and OD-ZnO components was effectively inhibited. The enhanced charge separation in the heterojunction was then further understood by the time-resolved transient PL spectroscopy, which were monitored at 460 nm under 400 nm excitation. As can be seen in Fig. 4b, the emission decay data could be normalized and fitted by triexponential kinetics ($I = A_1 e^{-t/\tau_1} + A_2 e^{-t/\tau_2} + A_3 e^{-t/\tau_3}$) for which three components were derived. Interestingly, for all three components, the CN-10/OD-ZnO heterojunction ($\tau_1 = 2.98$ ns, $A_1 = 33.2\%$; $\tau_2 = 9.43$ ns, $A_2 = 53.1\%$; $\tau_3 = 53.71$ ns, $A_3 = 13.7\%$) yielded much longer emission lifetimes compared with g-C₃N₄ nanosheets ($\tau_1 = 1.07$ ns, $A_1 = 34.5\%$; $\tau_2 = 4.07$ ns, $A_2 = 50.2\%$; $\tau_3 = 18.84$ ns, $A_3 = 15.3\%$). Moreover, an overall comparison of the emission decay behavior was deduced by the intensity-average lifetimes through the following equation [44]:

$$\tau = \frac{A_1 \tau_1^2 + A_2 \tau_2^2 + A_3 \tau_3^2}{A_1 \tau_1 + A_2 \tau_2 + A_3 \tau_3}$$

The results showed that, after coupling with OD-ZnO, the $\langle\tau\rangle$ value of g-C₃N₄ nanosheets significantly increased from 11.90 to 33.35 ns. The observed elongation of emission lifetime indicated that the charge recombination of g-C₃N₄ nanosheets in the heterojunction was inhibited, and thus the photoinduced electrons and holes could be more effectively separated and utilized in the photocatalytic processes.

The photocatalytic degradation performances of different samples were evaluated under visible-light irradiation ($\lambda > 420$ nm) using 4-CP as a typical colorless non-dye organic contaminant. As shown in Figs. 5a and S11, in the dark-adsorption stage, the g-C₃N₄/ZnO nanocomposite samples showed better adsorption abilities than the solely ZnO and g-C₃N₄ samples, which may be attributed to their increased surface areas. Under visible-light irradiation, the C-ZnO reference showed very low activity in photodegradation due to its poor visible-light absorption capacity, and only about 2.8% of 4-CP was degraded after 90 min of irradiation. The degradation ratio of 4-CP was 34.2 and 64.2% for g-C₃N₄ and OD-ZnO after 90 min, respectively, suggesting better degradation activities of OD-ZnO than g-C₃N₄. When g-C₃N₄ was coupled with C-ZnO, the degradation activity slightly increased compared to pure g-C₃N₄. However, when g-C₃N₄ was coupled with OD-ZnO, the photodegradation activity was significantly enhanced. The CN-10/OD-ZnO sample exhibited the highest activity and nearly 95% of 4-CP could be degraded after only 60 min of irradiation. The degra-

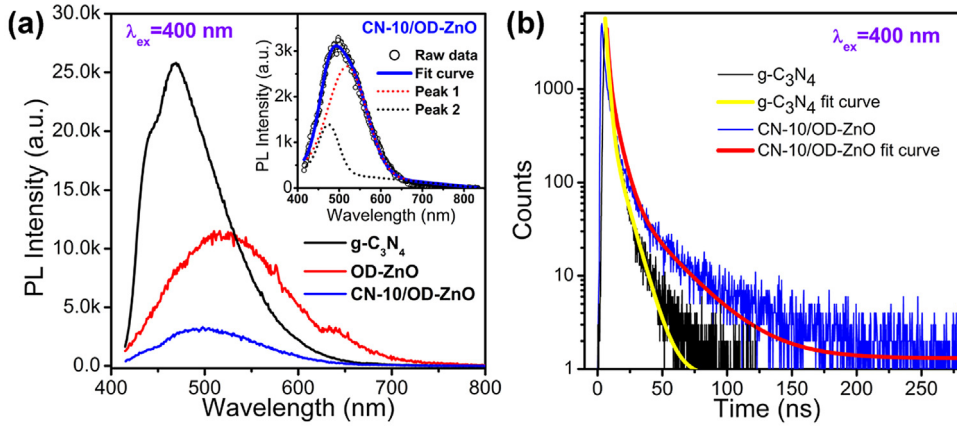


Fig. 4. (a) Steady-state PL measurements of $g\text{-C}_3\text{N}_4$, OD-ZnO and CN-10/OD-ZnO under 400 nm excitation; (b) time-resolved PL decay and their fitting curves monitored at 460 nm under the excitation of 400 nm for $g\text{-C}_3\text{N}_4$ and CN-10/OD-ZnO samples.

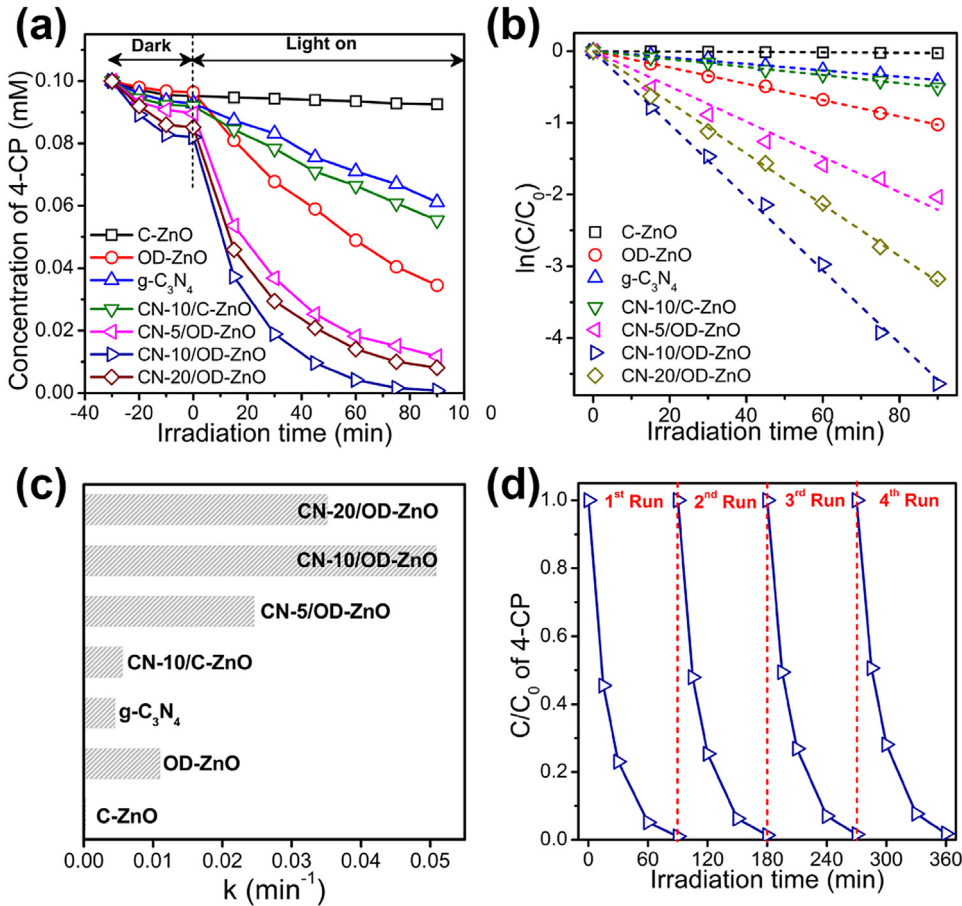


Fig. 5. (a) Photocatalytic degradation of 4-CP under visible-light irradiation ($\lambda > 420$ nm) over different samples; (b) pseudo first-order kinetic fitting and (c) the determined apparent rate constants (k , min^{-1}) of the tested samples; (d) cycle performance of CN-10/OD-ZnO for the photodegradation of 4-CP.

dation data could be fitted by pseudo first-order kinetic equation (Fig. 5b) and the determined apparent rate constants of the tested samples are displayed in Fig. 5c, clearly demonstrating the photocatalytic activity order of the samples. The CN-10/OD-ZnO sample showed the highest rate constant of 0.0509 min^{-1} , about 11 and 4.6 times higher than that of pure $g\text{-C}_3\text{N}_4$ and OD-ZnO, respectively. Stability tests were also performed by recycling the photocatalysts for the photodegradation of 4-CP over CN-10/OD-ZnO sample under visible light irradiation. As shown in Fig. 5d, only a slight loss of the photocatalytic activity of the sample was observed in

four cycles. Moreover, consider that the degradation process may involve the formation of various intermediates and by-products such as *p*-benzoquinone and hydroquinone [45], we also performed a total organic carbon (TOC) analysis of the 4-CP degradation process over CN-10/OD-ZnO sample. As shown in Fig. S12, over 90% of 4-CP was completely mineralized after irradiation for 280 min, indicating the most active sample could also lead to a high mineralization of 4-CP, which is consistent with some previous studies [46,47].

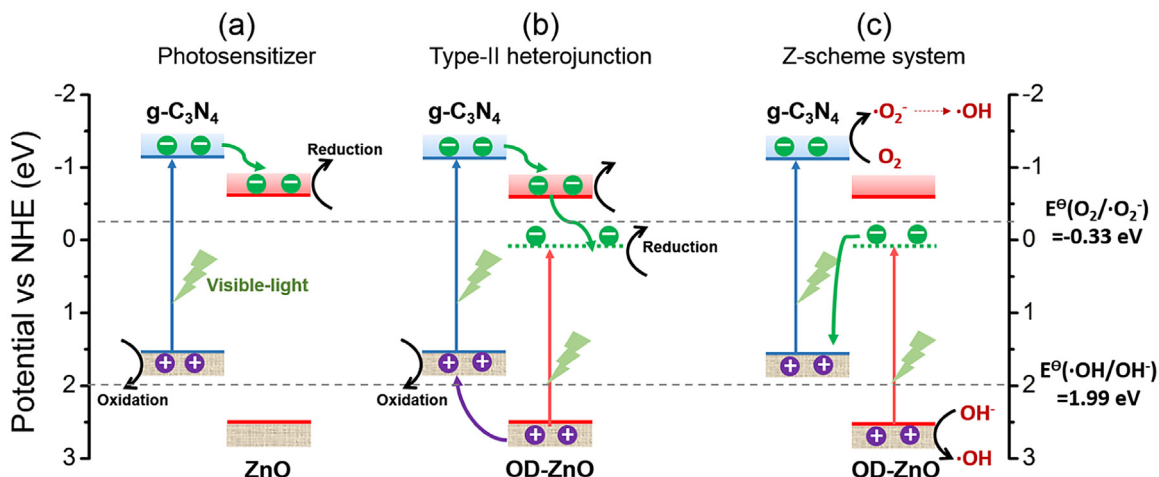


Fig. 6. (a) Schematic illustration of the charge-transfer in $\text{g-C}_3\text{N}_4$ coupled with defect-free ZnO under visible-light; (b, c) schematic illustration of two possible mechanisms for charge-transfer and photocatalysis in $\text{g-C}_3\text{N}_4$ coupled with oxygen-defective ZnO under visible-light, i.e. type II heterojunction (b) and Z-scheme system (c).

Though enhanced visible-light photocatalytic of the $\text{g-C}_3\text{N}_4/\text{OD-ZnO}$ heterojunction could be related to the improved charge generation and separation, as evidenced by optical and electrochemical measurements demonstrated above, it is still necessary to ascertain the migrated channel of the photoinduced electrons and holes to reveal the photocatalytic mechanisms. When $\text{g-C}_3\text{N}_4$ was coupled with C-ZnO with few oxygen defects, the enhanced photocatalytic activity could be simply understood by the so called “photosensitizer” mechanism [48], i.e. the $\text{g-C}_3\text{N}_4$ served as a sensitizer for visible-inert ZnO , as illustrated in Fig. 6a. Under visible-light irradiation, the electrons in VB of $\text{g-C}_3\text{N}_4$ would be excited to the CB of $\text{g-C}_3\text{N}_4$, and further transferred to the CB of ZnO . The electrons gathered in the CB of ZnO and the holes left behind in the VB of $\text{g-C}_3\text{N}_4$ would lead to the occurrence of reduction and oxidation reactions, respectively. Such spatial separation of the photoinduced electrons/holes by this “photosensitizer” mechanism reduced the electron-hole recombination ratio, which promoted the subsequent redox reactions leading to a higher visible-light photocatalytic performance of the $\text{g-C}_3\text{N}_4/\text{C-ZnO}$ heterostructures compared to pure $\text{g-C}_3\text{N}_4$, even though C-ZnO was visible-light inert.

When $\text{g-C}_3\text{N}_4$ was coupled with OD-ZnO, the migrated channel of the photoinduced electrons and holes became complex since both $\text{g-C}_3\text{N}_4$ and OD-ZnO could be excited under visible light. Two possible mechanisms for the charge transfer and photocatalytic process in the $\text{g-C}_3\text{N}_4/\text{OD-ZnO}$ heterojunction were proposed, i.e. type II heterojunction and Z-scheme system. In detail, for type-II heterojunction (Fig. 6b), the excited electrons in CB of $\text{g-C}_3\text{N}_4$ would transfer to the CB of OD-ZnO and may further be trapped in the V_0 -level with lower energy, while the holes in the VB of OD-ZnO would transfer to the VB of $\text{g-C}_3\text{N}_4$. As a result, photoinduced electrons and holes would be accumulated in the V_0 -level of OD-ZnO and VB of $\text{g-C}_3\text{N}_4$, respectively. However, for the Z-scheme system in Fig. 6c, the photoinduced electrons trapped in the V_0 -level of OD-ZnO would directly recombine with the holes in the VB of $\text{g-C}_3\text{N}_4$ at the heterojunction interface, and thereby inhibited the recombination in both $\text{g-C}_3\text{N}_4$ and OD-ZnO components, thus leading to the accumulation of photoinduced electrons and holes in the CB of $\text{g-C}_3\text{N}_4$ and VB of ZnO , respectively, in contrast to the situation for type-II heterojunction. These two mechanisms were both beneficial for the charge generation and separation in the heterojunction, which would result in the enhanced photocurrent as well as prolonged charge lifetime. Therefore, they could not be identified by optical and electrochemical measurements.

According to the band structures of $\text{g-C}_3\text{N}_4$ and OD-ZnO, the photoinduced holes on $\text{g-C}_3\text{N}_4$ cannot oxidize the adsorbed H_2O molecules to $\cdot\text{OH}$ because the VB potential of $\text{g-C}_3\text{N}_4$ (+1.57 eV vs. NHE) [49] is less positive than the standard redox potential $E(\cdot\text{OH}/\text{OH}^-)$ (1.99 eV vs. NHE, pH = 7) [50]. Because the photoinduced electrons were trapped in the V_0 -level of OD-ZnO, it was hard to reduce the adsorbed O_2 molecules because the V_0 -level potential of OD-ZnO (ca. 0.1 eV vs. NHE) is more positive than the standard redox potential $E(\text{O}_2/\cdot\text{O}_2^-)$ (-0.33 eV vs. NHE, pH = 7) [50]. If $\text{g-C}_3\text{N}_4/\text{OD-ZnO}$ was a type-II heterojunction, the electrons and holes accumulated in the V_0 -level of OD-ZnO and VB of $\text{g-C}_3\text{N}_4$ would not be favorable for the generation of $\cdot\text{O}_2^-$ and $\cdot\text{OH}$, respectively. However, if a Z-scheme system was constructed for the heterojunction, the generation and accumulation of electrons in the CB of $\text{g-C}_3\text{N}_4$ and holes in VB of ZnO would be promoted in both cases owing to the interfacial recombination, leading to the enhanced generation of $\cdot\text{O}_2^-$ and $\cdot\text{OH}$. Therefore, the detection of surface generated reactive species such as $\cdot\text{O}_2^-$ and $\cdot\text{OH}$ on different photocatalysts should be an effective approach to determine the photocatalytic mechanism.

DMPO in methanol was used for the detection of $\cdot\text{O}_2^-$ generated on the surface of photocatalysts through ESR signals of DMPO- $\cdot\text{O}_2^-$ [51], as shown in Fig. 7a. As expected, OD-ZnO shows weak signals since most photoinduced electrons were trapped in the V_0 -level below $E(\text{O}_2/\cdot\text{O}_2^-)$, while $\text{g-C}_3\text{N}_4$ shows obvious signals. CN-10/C-ZnO sample exhibited signals with comparable intensity to $\text{g-C}_3\text{N}_4$ since $\cdot\text{O}_2^-$ could also be generated on CB of ZnO . The signals of CN-10/OD-ZnO have an obvious larger intensity compared to that of other samples, indicating that the generation of $\cdot\text{O}_2^-$ was enhanced on the $\text{g-C}_3\text{N}_4/\text{OD-ZnO}$ heterojunction. In addition, the transformation percentage of NBT degraded by different samples under visible light was also evaluated, which could be used to quantitatively determine the generated $\cdot\text{O}_2^-$ radicals in the photocatalytic process [52], and the results are shown in Fig. S13. As expected, the order of degradation percentage of NBT is consistent with the results from DMPO trapping experiments. On the other hand, hydroxyl radicals ($\cdot\text{OH}$) generated on the surface of different photocatalysts were also detected by the fluorescence spectrometer with a 5×10^{-4} mol L⁻¹ basic solution of terephthalic acid (TA) as a probe molecule [53], as shown in Fig. 7b. TA readily reacts with $\cdot\text{OH}$ to produce a highly fluorescent product, i.e., 2-hydroxyterephthalic acid, whose PL peak centered at ca. 425 nm and the intensity was in proportion to the amount of $\cdot\text{OH}$ radicals formed in water. Though $\cdot\text{OH}$ cannot be produced on the VB of $\text{g-C}_3\text{N}_4$, a weak PL peak was observed for $\text{g-C}_3\text{N}_4$ sample since the $\cdot\text{O}_2^-$ generated on

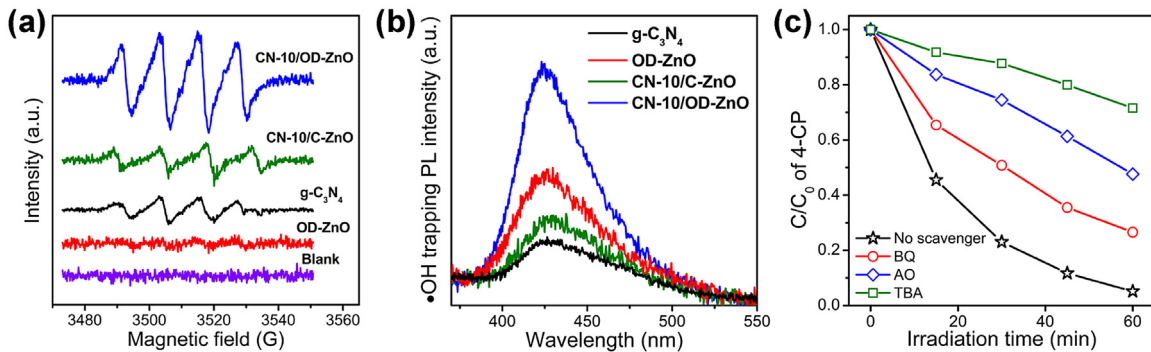


Fig. 7. (a) DMPO spin-trapping ESR signals for DMPO-•O₂⁻ of different samples in methanol dispersion upon visible-light irradiation for 30 s; (b) •OH trapping PL spectra of different samples with TA solution upon visible-light irradiation for 30 min; (c) photocatalytic degradation of 4-CP over CN-10/OD-ZnO sample under visible-light irradiation in the presence of different scavengers.

CB can further transfer into •OH (•O₂⁻ + H₂O + e⁻ → HO₂⁻ + OH⁻; HO₂⁻ + e⁻ → •OH + 2OH⁻). The CN-10/C-ZnO sample showed a slightly higher PL intensity because of the improved charge separation. The OD-ZnO sample shows a more higher PL intensity originated from the water oxidation by the photoinduced holes on VB of OD-ZnO (h⁺ + OH⁻ → •OH). The CN-10/OD-ZnO sample exhibited the highest PL intensity, indicating that the •OH generation was also promoted on the g-C₃N₄/OD-ZnO heterojunction. The efficient production of •O₂⁻ and •OH on the g-C₃N₄/OD-ZnO heterojunction cannot be well explained by the type-II heterojunction according to the energy band structures in Fig. 6b. Therefore, the charge separation by the heterojunction in the current work should be attributed to the Z-scheme mechanism.

The contributions of reactive species including h⁺, •O₂⁻ and •OH to the photocatalytic reaction were also evaluated by introducing some scavengers. Ammonium oxalate (AO), benzoquinone (BQ) and *tert*-butyl alcohol (TBA) were employed as scavengers for h⁺, •O₂⁻ and •OH [54], respectively to investigated their influences on the photodegradation of 4-CP, as shown in Fig. 7c. The photocatalytic activity of the CN-10/OD-ZnO sample was greatly suppressed by the addition of TBA, indicating that •OH was the main active species in the photocatalytic reaction. Moreover, the decrease in the photocatalytic activity was also observed by the addition of AO as h⁺ scavenger and BQ as O₂⁻ scavenger, respectively, and h⁺ played a more important role. The different contribution of reactive species could be connected with the previously proposed degradation pathway of 4-CP as shown in Fig. S14, which indicates that •OH plays the most critical roles in the formation of various intermediates and the final complete mineralization of 4-CP [45,47,55]. These results were also consistent with the proposed Z-scheme mecha-

nism since it implied that the holes were preferably accumulated on the VB of ZnO, which subsequently led to the formation of •OH.

Based on the above discussion, the roles of oxygen vacancies of OD-ZnO in mediating the Z-scheme charge separation of g-C₃N₄/OD-ZnO heterojunction under visible light illumination could be summarized by the following two aspects. On the one hand, the V_O generated isolated level below the CB of OD-ZnO played the role of “band gap narrowing”, increasing the visible-light absorption ability of the heterojunction. On the other hand, under visible-light illumination, the photoinduced electrons generated and trapped in the V_O level of OD-ZnO could directly recombine with the photoinduced holes in VB of g-C₃N₄ at the heterojunction interface, consequently, the Z-scheme charge separation was constructed in the g-C₃N₄/OD-ZnO heterojunction.

Z-scheme systems were considered as efficient photocatalysts for hydrogen evolution as it can provide high redox overpotentials for both oxidation and reduction reactions. In this work, photocatalytic H₂ evolution activities of the as-prepared samples were also evaluated under visible-light ($\lambda > 420$ nm) irradiation using 10 vol% TEOA solutions as sacrificial agents. Pt cocatalyst (1.0 wt%) was loaded by an in-situ photochemical deposition. g-C₃N₄/Pt showed visible light activity for H₂ evolution, however, the rate was comparatively low (ca. 6.5 $\mu\text{mol h}^{-1}$) due to the high recombination rate in g-C₃N₄, in accordance with some previous reports [56,57]. OD-ZnO sample showed no obvious activity for H₂ evolution under visible light even after loading with Pt due to the low potential of the photoinduced electrons. The Pt loaded g-C₃N₄/OD-ZnO heterostructures showed enhanced H₂ evolution compared to pure g-C₃N₄, and the CN-20/OD-ZnO sample (20 wt% g-C₃N₄) achieved an optimal H₂ evolution rate of 32.2 $\mu\text{mol h}^{-1}$, about 5 times than that of pure g-C₃N₄ even though the OD-ZnO compo-

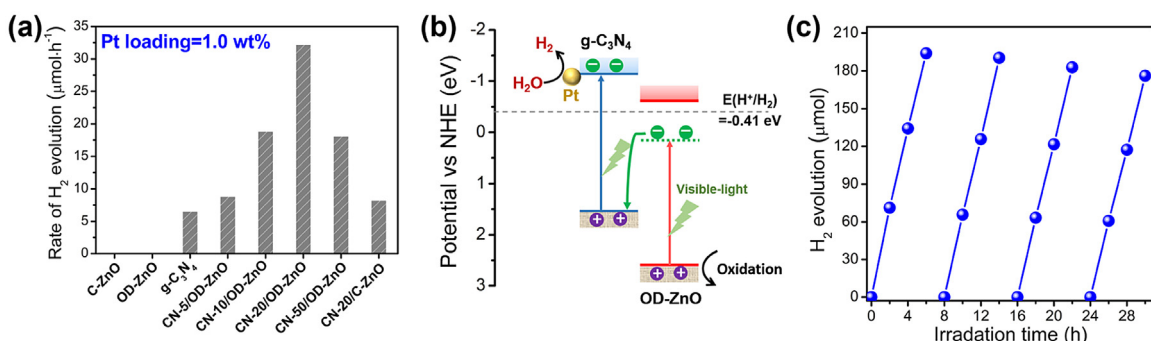


Fig. 8. (a) The rate of H₂ evolution on different samples loaded with 1 wt% Pt as a cocatalyst under visible-light irradiation ($\lambda > 420$ nm); (b) schematic illustration of the visible-light photocatalytic H₂ evolution on the g-C₃N₄/OD-ZnO heterojunction through a Z-scheme mechanism; (c) time-dependent photocatalytic H₂ evolution for CN-20/OD-ZnO sample in four cycles; the light was turned off for 2 h among cycles and the reaction system was bubbled with Ar for 30 min to remove the H₂ inside.

ment itself could not produce H_2 under visible-light. In addition, the light intensity dependent H_2 evolution rate of CN-20/OD-ZnO sample was also evaluated. As shown in Fig. S15, the photocatalytic H_2 evolution rate was approximately proportional to light intensity in the range of $0.1\text{--}2\text{ mW cm}^{-2}$, implying that the photoexcited electrons and holes were well separated and consumed in the subsequent surface reactions [58]. The enhanced visible light H_2 evolution of the $g\text{-}C_3N_4$ /OD-ZnO heterojunction should be also attributed to the V_0 -mediated Z-scheme charge separation, as shown in Fig. 8b. The interfacial recombination of the photoinduced electrons trapped in the V_0 -level of OD-ZnO with the photoinduced holes in the VB of $g\text{-}C_3N_4$ promoted the spatial charge separation. Electrons would be efficiently generated and accumulated in CB of $g\text{-}C_3N_4$ and further injected into Pt cocatalyst to trigger the H_2 evolution reaction, while the holes accumulated in VB of OD-ZnO could provide higher overpotential for the oxidation of sacrificial agents. It was noticed that the H_2 evolution rates achieved herein ($322\text{ }\mu\text{mol h}^{-1}\text{ g}^{-1}$) by the $g\text{-}C_3N_4$ /OD-ZnO heterojunction were smaller than some heterojunctions of $g\text{-}C_3N_4$ /metal sulfide such as $g\text{-}C_3N_4$ /CdS ($4152\text{ }\mu\text{mol h}^{-1}\text{ g}^{-1}$) [59] and $g\text{-}C_3N_4$ /NiS ($447.7\text{ }\mu\text{mol h}^{-1}\text{ g}^{-1}$) [60], but comparable or even higher than some $g\text{-}C_3N_4$ /metal oxide heterojunctions under visible light illumination ($\lambda > 420\text{ nm}$), such as $g\text{-}C_3N_4$ /N–CeO_x ($292.5\text{ }\mu\text{mol h}^{-1}\text{ g}^{-1}$) [61], $g\text{-}C_3N_4$ /TiO₂ ($224\text{ }\mu\text{mol h}^{-1}\text{ g}^{-1}$) [62] and $g\text{-}C_3N_4$ /WO₃ ($28.4\text{ }\mu\text{mol h}^{-1}\text{ g}^{-1}$) [63], etc. Here, we also report for the first time, the oxygen-defects mediated $g\text{-}C_3N_4$ -based Z-scheme system for enhanced visible-light H_2 evolution.

Recycling test was performed on the H_2 evolution performance of the CN-20/OD-ZnO sample to evaluate the stability of the heterojunction under visible-light, as shown in Fig. 8c. After four recycles, the average H_2 evolution rate decreased from 32.2 to $29.1\text{ }\mu\text{mol h}^{-1}$, indicating the acceptable stability and reusability of the catalysts. The decrease of photocatalytic activity could be mainly attributed to photocorrosion reaction of ZnO caused by the photoinduced holes ($ZnO + 2h^+ \rightarrow Zn^{2+} + 0.5O_2$) [64]. The XRD of the sample after 5 cycles is presented in Fig. S16, which demonstrated that no detectable phase or composition change occurred during the photocatalytic processes. Moreover, the as-synthesized $g\text{-}C_3N_4$ /OD-ZnO photocatalysts had the merit of good sedimentation ability, which made for easy recovery and separation after usage. After free sedimentation for 20 min, most of the $g\text{-}C_3N_4$ /OD-ZnO photocatalysts have separated from the original suspension (Fig. S17a) and accumulated at the bottom of vial. In contrast, the pure $g\text{-}C_3N_4$ sheets were still well-dispersed in the solution (Fig. S17b), suggesting that the assembling of $g\text{-}C_3N_4$ sheets into a core-shell heterojunction was beneficial for photocatalyst separation. Nevertheless, more attention should be paid to the photostability of the $g\text{-}C_3N_4$ -based Z-scheme photocatalysts since oxidative holes are accumulated on the other components.

It was noticed that CN-10/OD-ZnO and CN-20/OD-ZnO showed optimum photocatalytic activity in degradation of 4-CP and hydrogen evolution, respectively. The difference in optimal values of $g\text{-}C_3N_4$ ratio for degradation and hydrogen evolution could be explained by the different photocatalytic mechanisms in these two cases. The degradation of 4-CP occurred in an oxygen-bearing solution. Therefore, the photoinduced electrons accumulated on $g\text{-}C_3N_4$ surface were captured by O_2 to form $\bullet O_2^-$, and highly oxidative h^+ and $\bullet OH$ were generated on OD-ZnO surfaces. These active species were all involved in the oxidation of 4-CP. According to the results in Fig. 8c, $\bullet OHs$ on ZnO surfaces were the main active species in the oxidation process, while $\bullet O_2^-$ generated on $g\text{-}C_3N_4$ surface showed weaker effect on degradation of 4-CP. Therefore, the CN-10/OD-ZnO sample with a higher ZnO ratio exhibited optimum degradation activity. On the other hand, when the hydrogen evolution occurred in an oxygen-free solution, the photoinduced electrons accumulated on $g\text{-}C_3N_4$ surfaces were injected into Pt co-catalyst to trigger

the hydrogen evolution, while the holes accumulated on OD-ZnO surfaces were consumed in the oxidation of sacrificial agents. In summary, the active species on the surface of OD-ZnO in the Z-scheme system participated directly in the oxidation of 4-CP, but did not involve in hydrogen evolution reaction. Therefore, the CN-20/OD-ZnO sample with a higher $g\text{-}C_3N_4$ ratio exhibited optimum H_2 evolution activity.

4. Conclusion

In summary, heterojunction photocatalysts were fabricated by coupling $g\text{-}C_3N_4$ nanosheets with oxygen-defective ZnO nanorods. The rich oxygen vacancies in OD-ZnO play dual-function roles of improving visible-light absorption and mediating the efficient Z-scheme charge separation of the $g\text{-}C_3N_4$ /OD-ZnO heterojunction, leading to their enhanced visible-light photocatalytic performances for degradation of 4-chlorophenol as well as H_2 evolution. The present work demonstrated an effective strategy for construction of novel visible-light-driven Z-scheme photocatalysts by taking advantage of oxygen defects in semiconductors.

Acknowledgements

This work was financially supported by the National Science Foundation of China (Nos. 51234003 and 51374138), National Science Foundation of Jiangsu Province (BK20160328) and National Key Technology Research and Development Program of China (2013BAC14B02). Jing Wang is grateful for the scholarship from China Scholarship Council (No. 201506210232).

Appendix A. Supplementary data

Supplementary data associated with this article can be found, in the online version, at <http://dx.doi.org/10.1016/j.apcatb.2017.01.067>.

References

- [1] W.J. Ong, L.L. Tan, Y.H. Ng, S.T. Yong, S.P. Chai, *Chem. Rev.* 116 (2016) 7159–7329.
- [2] G. Mamba, A. Mishra, *Appl. Catal. B: Environ.* 198 (2016) 347–377.
- [3] J. Zhang, F. Guo, X. Wang, *Adv. Funct. Mater.* 23 (2013) 3008–3014.
- [4] Y. Zhang, T. Mori, J. Ye, M. Antonietti, *J. Am. Chem. Soc.* 132 (2010) 6294–6295.
- [5] Y. Kang, Y. Yang, L.C. Yin, X. Kang, G. Liu, H.M. Cheng, *Adv. Mater.* 27 (2015) 4572–4577.
- [6] K. Wang, Q. Li, B. Liu, B. Cheng, W. Ho, J. Yu, *Appl. Catal. B: Environ.* 176 (2015) 44–52.
- [7] C. Chang, Y. Fu, M. Hu, C. Wang, G. Shan, L. Zhu, *Appl. Catal. B: Environ.* 142 (2013) 553–560.
- [8] P. Zhou, J. Yu, M. Jaroniec, *Adv. Mater.* 26 (2014) 4920–4935.
- [9] Y. Wang, Q. Wang, X. Zhan, F. Wang, M. Safdar, J. He, *Nanoscale* 5 (2013) 8326–8339.
- [10] J. Yan, H. Wu, H. Chen, Y. Zhang, F. Zhang, S.F. Liu, *Appl. Catal. B: Environ.* 191 (2016) 130–137.
- [11] J.C. Wang, H.-C. Yao, Z.Y. Fan, L. Zhang, J.S. Wang, S.Q. Zang, Z.J. Li, *ACS Appl. Mat. Interfaces* 8 (2016) 3765–3775.
- [12] Y. Hong, Y. Jiang, C. Li, W. Fan, X. Yan, M. Yan, W. Shi, *Appl. Catal. B: Environ.* 180 (2016) 663–673.
- [13] Q. Sun, K. Lv, Z. Zhang, M. Li, B. Li, *Appl. Catal. B: Environ.* 164 (2015) 420–427.
- [14] Z. Jin, N. Murakami, T. Tsubota, T. Ohno, *Appl. Catal. B: Environ.* 150 (2014) 479–485.
- [15] W. Yu, D. Xu, T. Peng, *J. Mater. Chem. A* 3 (2015) 19936–19947.
- [16] Y. Bai, P.-Q. Wang, J.-Y. Liu, X.-J. Liu, *RSC Adv.* 4 (2014) 19456–19461.
- [17] D. Zheng, C. Pang, X. Wang, *Chem. Comm.* 51 (2015) 17467–17470.
- [18] X. Yang, H. Tang, J. Xu, M. Antonietti, M. Shalom, *ChemSusChem* 8 (2015) 1350–1358.
- [19] K. Kondo, N. Murakami, C. Ye, T. Tsubota, T. Ohno, *Appl. Catal. B: Environ.* 142 (2013) 362–367.
- [20] S. Kumar, A. Baruah, S. Tonda, B. Kumar, V. Shanker, B. Sreedhar, *Nanoscale* 6 (2014) 4830–4842.
- [21] X. Jia, M. Tahir, L. Pan, Z.-F. Huang, X. Zhang, L. Wang, J.-J. Zou, *Appl. Catal. B: Environ.* 198 (2016) 154–161.
- [22] Y. Liu, R. Wang, Z. Yang, H. Du, Y. Jiang, C. Shen, K. Liang, A. Xu, *Chin. J. Catal.* 36 (2015) 2135–2144.

[23] Y. He, L. Zhang, M. Fan, X. Wang, M.L. Walbridge, Q. Nong, Y. Wu, L. Zhao, *Sol. Energy Mater. Sol. Cells* 137 (2015) 175–184.

[24] H. Cheng, J. Hou, O. Takeda, X.M. Guo, H. Zhu, *J. Mater. Chem. A* 3 (2015) 11006–11013.

[25] K. Li, X. Zeng, S. Gao, L. Ma, Q. Wang, H. Xu, Z. Wang, B. Huang, Y. Dai, J. Lu, *Nano Res.* 9 (2016) 1–14.

[26] J. Wang, S. Hou, H. Chen, L. Xiang, *J. Phys. Chem. C* 118 (2014) 19469–19476.

[27] Y. Zhang, J. Liu, G. Wu, W. Chen, *Nanoscale* 4 (2012) 5300–5303.

[28] X. Xu, C. Xu, Y. Lin, J. Li, J. Hu, *J. Phys. Chem. C* 117 (2013) 24549–24553.

[29] Ü. Özgür, Y.I. Alivov, C. Liu, A. Teke, M. Reschchikov, S. Dogan, V. Avrutin, S.J. Cho, H. Morkoc, *J. Appl. Phys* 98 (2005) 041301.

[30] K. Kotsis, V. Staemmler, *Phys. Chem. Chem. Phys.* 8 (2006) 1490–1498.

[31] X. Zou, J. Liu, J. Su, F. Zuo, J. Chen, P. Feng, *Chem. Eur. J.* 19 (2013) 2866–2873.

[32] A.B. Djurišić, Y.H. Leung, *Small* 2 (2006) 944–961.

[33] Y. Zheng, C. Chen, Y. Zhan, X. Lin, Q. Zheng, K. Wei, J. Zhu, Y. Zhu, *Inorg. Chem.* 46 (2007) 6675–6682.

[34] C. Pan, J. Xu, Y. Wang, D. Li, Y. Zhu, *Adv. Funct. Mater.* 22 (2012) 1518–1524.

[35] X. Li, J. Zhang, L. Shen, Y. Ma, W. Lei, Q. Cui, G. Zou, *Appl. Phys. A* 94 (2009) 387–392.

[36] X. She, H. Xu, Y. Xu, J. Yan, J. Xia, L. Xu, Y. Song, Y. Jiang, Q. Zhang, H. Li, *J. Mater. Chem. A* 2 (2014) 2563–2570.

[37] H. Zeng, G. Duan, Y. Li, S. Yang, X. Xu, W. Cai, *Adv. Funct. Mater.* 20 (2010) 561–572.

[38] P. Camarda, F. Messina, L. Vaccaro, S. Agnello, G. Buscarino, R. Schneider, R. Popescu, D. Gerthsen, R. Lorenzi, F.M. Gelardi, *Phys. Chem. Chem. Phys.* 18 (2016) 16237–16244.

[39] K. Kodama, T. Uchino, *J. Appl. Phys* 111 (2012) 093525.

[40] L. Zhang, L. Yin, C. Wang, N. Lun, Y. Qi, D. Xiang, *J. Phys. Chem. C* 114 (2010) 9651–9658.

[41] Y. Zheng, L. Zheng, Y. Zhan, X. Lin, Q. Zheng, K. Wei, *Inorg. Chem.* 46 (2007) 6980–6986.

[42] K. Vanheusden, W. Warren, C. Seager, D. Tallant, J. Voigt, B. Gnade, *J. Appl. Phys.* 79 (1996) 7983–7990.

[43] H.-L. Guo, Q. Zhu, X.-L. Wu, Y.-F. Jiang, X. Xie, A.W. Xu, *Nanoscale* 7 (2015) 7216–7223.

[44] Y.-C. Chen, Y.-C. Pu, Y.-J. Hsu, *J. Phys. Chem. C* 116 (2012) 2967–2975.

[45] K. Ji, H. Dai, J. Deng, H. Zang, H. Arandiyan, S. Xie, H. Yang, *Appl. Catal. B: Environ.* 168 (2015) 274–282.

[46] N. Nishiyama, Y. Fujiwara, K. Adachi, K. Inumaru, S. Yamazaki, *Appl. Catal. B: Environ.* 176 (2015) 347–353.

[47] M. Mylساamy, M. Mahalakshmi, N. Subha, A. Rajabhuvaranwari, V. Murugesan, *RSC Adv.* 6 (2016) 35024–35035.

[48] G. Wang, X. Yang, F. Qian, J.Z. Zhang, Y. Li, *Nano Lett.* 10 (2010) 1088–1092.

[49] L. Ge, C. Han, J. Liu, *Appl. Catal. B: Environ.* 108 (2011) 100–107.

[50] X. Li, J. Yu, M. Jaroniec, *Chem. Soc. Rev.* 45 (2016) 2603–2636.

[51] L. Yu, W. Chen, D. Li, J. Wang, Y. Shao, M. He, P. Wang, X. Zheng, *Appl. Catal. B: Environ.* 164 (2015) 453–461.

[52] Y. Hong, C. Li, G. Zhang, Y. Meng, B. Yin, Y. Zhao, W. Shi, *Chem. Eng. J.* 299 (2016) 74–84.

[53] J. Yu, W. Wang, B. Cheng, B.-L. Su, *J. Phys. Chem. C* 113 (2009) 6743–6750.

[54] X. Zheng, D. Li, X. Li, J. Chen, C. Cao, J. Fang, J. Wang, Y. He, Y. Zheng, *Appl. Catal. B: Environ.* 168 (2015) 408–415.

[55] B. Palanisamy, C.M. Babu, B. Sundaravel, S. Anandan, V. Murugesan, *J. hazard. Mater.* 252 (2013) 233–242.

[56] J. Chen, D. Zhao, Z. Diao, M. Wang, L. Guo, S. Shen, *ACS Appl. Mat. Interfaces* 7 (2015) 18843–18848.

[57] F. He, G. Chen, Y. Yu, Y. Zhou, Y. Zheng, S. Hao, *Chem. Comm.* 51 (2015) 6824–6827.

[58] K. Maeda, K. Domen, *J. Phys. Chem. Lett.* 1 (2010) 2655–2661.

[59] J. Zhang, Y. Wang, J. Jin, J. Zhang, Z. Lin, F. Huang, J. Yu, *ACS Appl. Mat. Interfaces* 5 (2013) 10317–10324.

[60] Z. Chen, P. Sun, B. Fan, Z. Zhang, X. Fang, *J. Phys. Chem. C* 118 (2014) 7801–7807.

[61] J. Chen, S. Shen, P. Wu, L. Guo, *Green Chem.* 17 (2015) 509–517.

[62] H. Yan, H. Yang, *J. Alloys Compd.* 509 (2011) L26–L29.

[63] G. Zhao, X. Huang, F. Fina, G. Zhang, J.T. Irvine, *Catal. Sci. Technol.* 5 (2015) 3416–3422.

[64] C. Han, M.-Q. Yang, B. Weng, Y.J. Xu, *Phys. Chem. Chem. Phys.* 16 (2014) 16891–16903.